Research Square

Preprints are preliminary reports that have not undergone peer review.
They should not be considered conclusive, used to inform clinical practice,
or referenced by the media as validated information.

Effects of Magneto-Mechanical Coupling on Enhanced Magnetic Memory Signals of Defective Coiled Tubing

Tianyu Huang

huangtianyu@stu.cdut.edu.cn

Chengdu University of Technology

Xu Luo

Chengdu University of Technology

Yu Li

Shenzhen KTC Technology Co., Ltd

An Mao

Chengdu University of Technology

Wenbo Jiang

Chengdu University of Technology

Ziying Li

Chengdu University of Technology

Article

Keywords: Enhanced magnetic memory, Coiled tubing, Magneto-mechanical coupling, Defect detection

Posted Date: June 4th, 2026

DOI: https://doi.org/10.21203/rs.3.rs-9854109/v1

License: This work is licensed under a Creative Commons Attribution 4.0 International License.
Read Full License

Additional Declarations: No competing interests reported.

Version of Record: A version of this preprint was published at Scientific Reports on August 25th, 2026.
See the published version at https://doi.org/10.1038/s41598-026-67712-6.

Effects of Magneto-Mechanical Coupling on Enhanced Magnetic Memory Signals of Defective Coiled Tubing

Tianyu Huang(https://orcid.org/0009-0001-7000-2568)[a], Xu Luo[a], Yu Li[b] An Mao[a], Wenbo Jiang[a], Ziying Li[a]

[a]*School of Mechanical and Electrical Engineering, Chengdu University of Technology, Chengdu, China*
[b]*Shenzhen KTC Technology Co., Ltd., Shenzhen, China*
*****e-mail: huangtianyu@stu.cdut.edu.cn*

Abstract—To investigate the evolution characteristics of enhanced magnetic memory signals in defective coiled tubing under magneto-mechanical coupling, CT130 coiled tubing specimens containing crack, pit, and perforation defects were tested under different stress states. The enhanced magnetic memory signals and corresponding characteristic parameters in defect regions were analyzed. The results show that the enhanced magnetic memory signals can effectively reflect the internal stress and damage evolution of defective coiled tubing. With the increase in crack length and depth, the characteristic parameters of magnetic signals exhibit an approximately linear increasing trend. When the crack depth increased from 0.5 mm to 4 mm, the tangential and normal characteristic parameters increased by 494.9% and 233.6%, respectively. When the crack length increased from 1 mm to 8 mm, the corresponding increases reached 263.7% and 161.9%, indicating that crack depth has a more significant influence on local magnetic field anomalies. In addition, the characteristic parameters exhibited distinct staged evolution behavior with increasing stress amplitude and reached local peak values near the elastic-plastic transition stage at 800 MPa. The characteristic parameters under unloading conditions were generally higher than those under online loading conditions, demonstrating that enhanced magnetic memory signals possess obvious historical memory effects. The results provide a reference for defect evaluation and stress state assessment of coiled tubing.

Keywords: Enhanced magnetic memory; Coiled tubing; Magneto-mechanical coupling; Defect detection;

1. INTRODUCTION

As a core equipment in petroleum engineering, coiled tubing (CT) enables continuous running and retrieval operations, overcoming the limitations of conventional segmented

tubing strings and significantly improving operational efficiency. During service, coiled tubing is subjected not only to complex loads such as axial tension and compression, circumferential torsion, and radial bending, but also to harsh working conditions including fluid erosion, wall wear, and formation extrusion. Under these conditions, various defects such as corrosion, wear, scratches, and fatigue damage are prone to occur, seriously affecting the operational safety of coiled tubing. Therefore, effective defect detection of coiled tubing is essential for preventing unexpected failures and ensuring operational safety.

Metal magnetic memory testing can be used to detect both early-stage damage and macroscopic defects in ferromagnetic materials. In recent years, extensive studies have been conducted on the influencing factors of magnetic memory signals. Li et al.[1] carried out full-scale fatigue tests on coiled tubing and confirmed the correlation between magnetic memory signals and fatigue damage. Duan et al.[2] quantitatively investigated the effects of stress state and initial magnetization state on magnetic field signals in 40Cr and Q235 steel specimens, and found that the magnetization state and tensile load exhibited a multi-valued functional relationship. Liu et al.[3] analyzed the effects of stress and excitation magnetic field on the surface magnetic field of 45# steel under offline conditions, revealing an interaction coupling effect between stress and excitation magnetic field on the tangential magnetic memory signal. Fu et al.[4] studied the influence of tensile stress on magnetic memory signals of Q345 steel specimens with different thicknesses and explained the differences in magnetic field evolution during the elastic-plastic stage. Ren et al.[5] focused on the magnetization reversal effect of Q235 steel under torsional loading and evaluated the relationship between leakage magnetic field and torque under different torque levels. Ni et al.[6] found that both the peak-to-peak value and peak value of the magnetic signal gradient were positively correlated with notch depth. Jia et al.[7] investigated the metal magnetic memory effect of X80 pipeline steel and analyzed the variation characteristics of magnetic field components under different tensile loads. Bai et al.[8] analyzed the nonlinear variation of normal magnetic signals along the stress concentration path in the elastic stage and compared it with the signal evolution in the plastic stage. Leng et al.[9] investigated the variation characteristics of magnetic memory signals in Q235 steel under different working loads and after unloading, and found a strong correlation between magnetic memory signals and working stress. Xu et al.[10] reported that the diameter of circular-hole defects was positively correlated with the average and maximum values of magnetic field gradient, while the degree of stress concentration was positively correlated with the maximum magnetic field intensity and the enclosed area between the magnetic field intensity curve and the horizontal axis. Xu et al.[11] further investigated the effects of heat treatment and external loading on magnetic memory testing results of Q235 steel, and found that stress-relief heat treatment reduced

the internal stress and weakened the leakage magnetic field intensity.

Although these studies provide useful references for coiled tubing inspection, most existing work has focused on conventional metal magnetic memory testing of materials such as Q235, X80, and Q345 steels. Targeted studies on coiled tubing materials under enhanced magnetic memory testing conditions are still limited. In addition, the combined effects and interactions of defect length, depth, and type have not been systematically analyzed, and the quantitative relationships between defect parameters and signal characteristic parameters remain unclear. Most studies on loading conditions have mainly considered a single stress amplitude or a single loading mode, while the magnetic field response during loading–unloading cycles and the elastic–plastic transition stage of coiled tubing under actual service conditions remains insufficiently investigated.

2. EXPERIMENTAL PROCEDURE AND SIGNAL CHARACTERISTIC ANALYSIS

2.1 Experimental System for Enhanced Magnetic Memory Testing

According to the requirements of online enhanced magnetic memory testing, the experimental system was established, as shown in Fig. 1. The system mainly consists of a stress loading device, a magnetic field generation device, a magnetic field measurement device, and a demagnetization device. The stress loading device is a DF13.305T electronic universal testing machine. The magnetic field generation device consists of a UU120 magnetic core and a 320-turn excitation coil, with the excitation current supplied by an ITECH IT6862A DC power supply. The magnetic field measurement device consists of a three-axis displacement platform and a CH-3600 Gaussmeter. The demagnetization device is a TC-4 desktop demagnetizer.

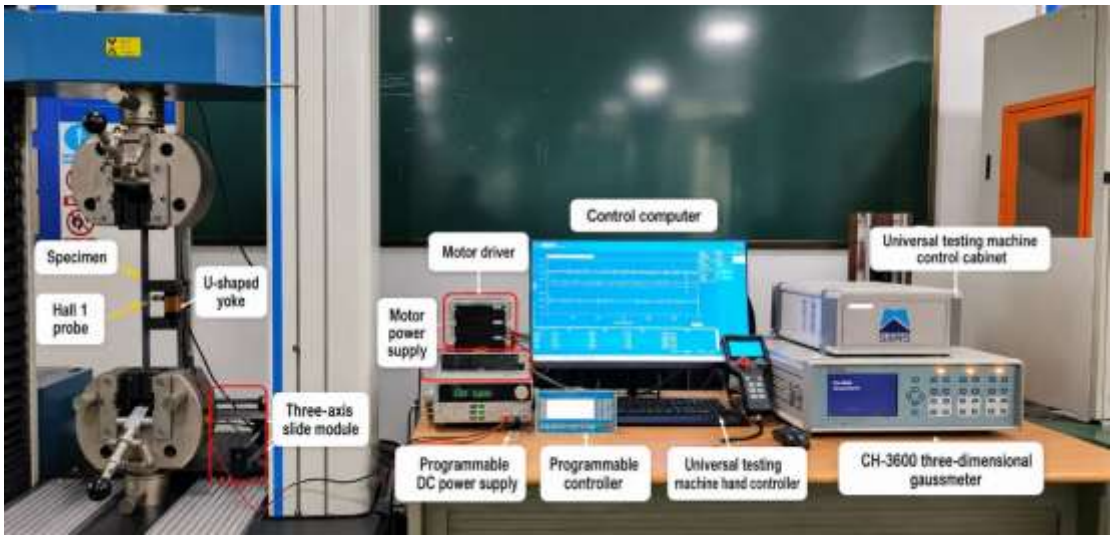


Fig. 1. Experimental system for online enhanced magnetic memory testing

2.2 Coiled Tubing Specimens with Defects

To evaluate the performance of the established enhanced magnetic memory testing system, CT130, a typical coiled tubing material, was selected as the test material[12]. The specimens were machined with three types of micro-defects at the center, as shown in Fig. 2. The specimen length, width, and thickness were 400 mm, 37 mm, and 4 mm, respectively.

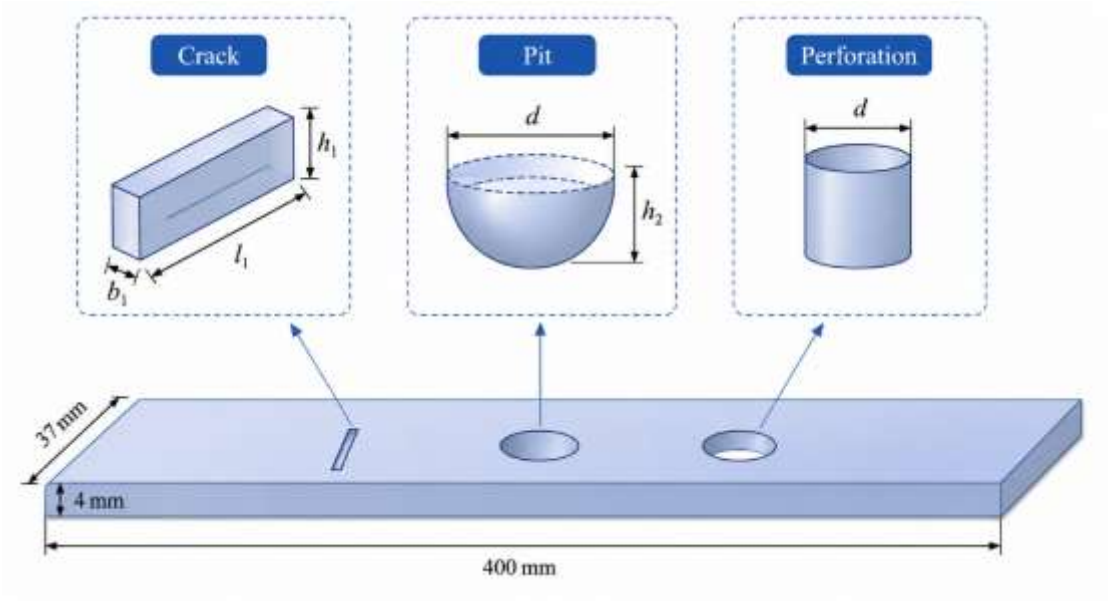


Fig. 2. Schematic diagram of the test specimen

To analyze the effects of defect characteristics and loading conditions on the detected signals during enhanced magnetic memory testing, relevant experiments were carried out using the established testing system. The experimental scheme is shown in Table 1.

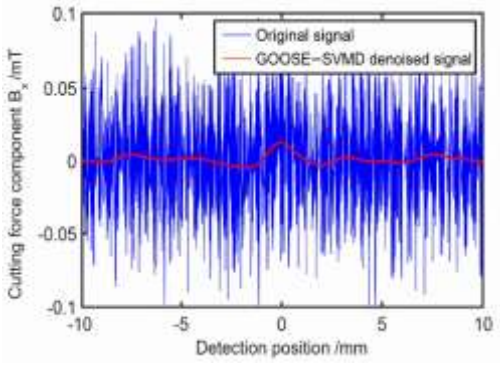
Table 1. Experimental scheme for analyzing influencing factors of enhanced magnetic memory testing signals

Test Item	Defect Type	Defect Size (mm)	Loading Condition	Stress Amplitude (MPa)
Effects of Crack Depth	Crack	2×0.6×0.5 2×0.6×1 2×0.6×1.5 2×0.6×2 2×0.6×2.5 2×0.6×3 2×0.6×3.5 2×0.6×4	Loading	1000
Effects of Crack Length	Crack	1×0.6×0.5 2×0.6×0.5 4×0.6×0.5	Loading	1000

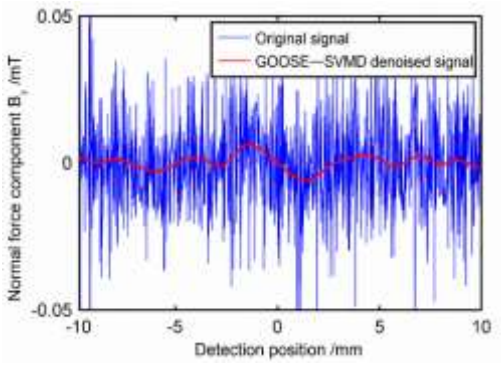
		6×0.6×0.5 8×0.6×0.5		
Effects of Defect Type	Perforation Pit Crack	Φ0.6×4 Φ1×0.5 2×0.6×0.5	Loading	1000
Effects of Stress Amplitude	Pit Crack	1×0.5 2×0.6×0.5	Loading	0,100,200…1000
Effects of Loading–Unloading Conditions	Perforation	Φ0.6×4	Loading Unloading	0,100,200…1000

2.3 Signal Denoising and Characteristic Parameter Extraction

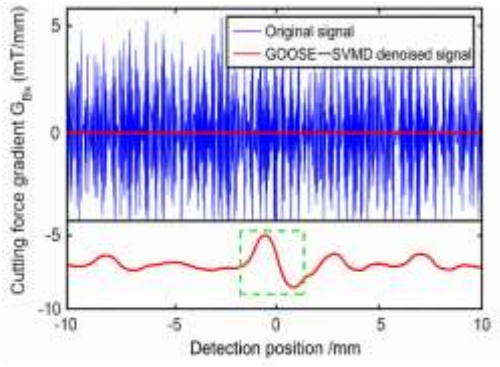
During enhanced magnetic memory testing, the detected signals are susceptible to environmental noise, which may reduce the accuracy of defect feature identification. To improve signal quality, a signal denoising method based on GOOSE (Golden Jackal Optimization Algorithm)-optimized SVMD (Successive Variational Mode Decomposition) was used to process the detected signals[13]. After denoising, the magnetic field anomaly characteristics in the defect region were well preserved, improving the stability and accuracy of characteristic parameter extraction. The denoising results are shown in Fig. 3.



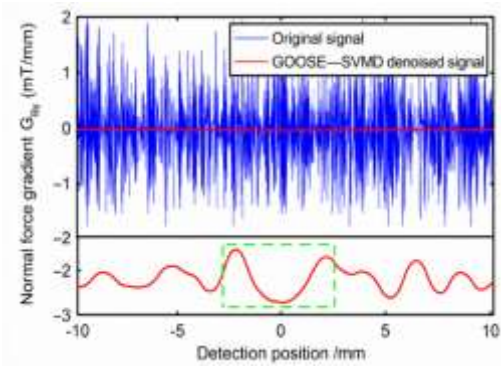
(a)Denoising result of B_x



(b)Denoising result of B_y



(c)Denoising result of G_{Bx}



(d)Denoising result of G_{By}

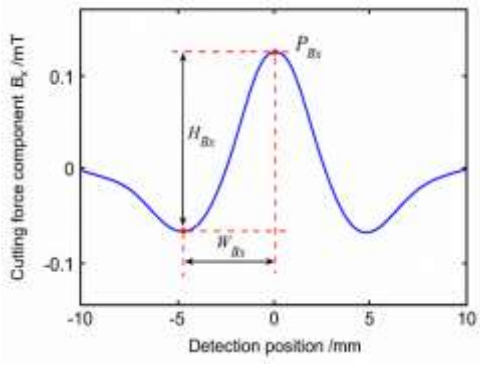
Fig. 3. Signal denoising results using the GOOSE-optimized SVMD algorithm

SVMD based on the GOOSE optimization algorithm can more effectively suppress noise interference in the detected signals. After processing, the signals become smoother, and the magnetic field anomaly characteristics in the defect region are more clearly identified.

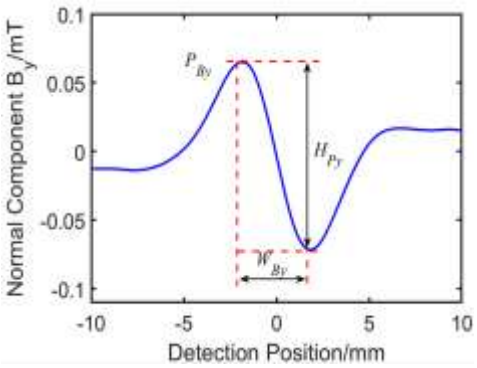
After a comprehensive analysis of the characteristic parameters of each component of the enhanced magnetic memory signals, the characteristic parameters and their symbols used in this study were defined, as listed in Table 2. Their calculation methods are illustrated in Fig. 4.

Table 2. Definitions of magnetic field signal characteristic parameters

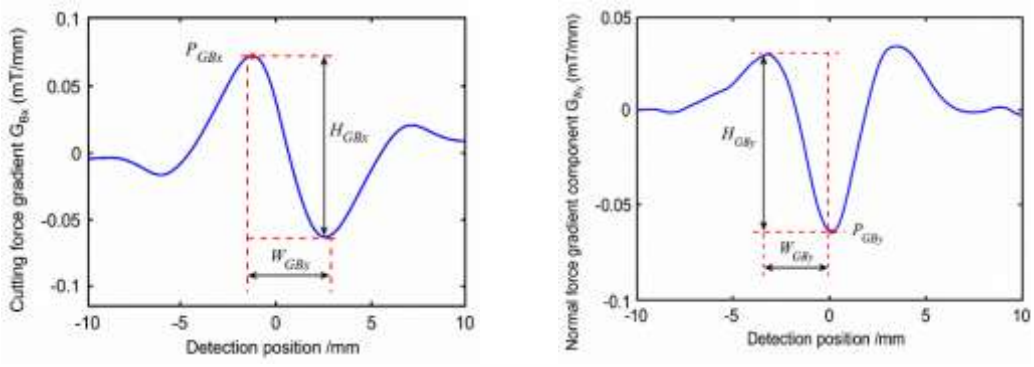
Magnetic Field Signal Component	Characteristic Parameter	Symbol
Tangential Component B_x	Peak Value	P_{Bx}
	Peak-to-Valley Value	H_{Bx}
	Peak-to-Peak Distance	W_{Bx}
Normal Component B_y	Peak Value	P_{By}
	Peak-to-Valley Value	H_{By}
	Peak-to-Peak Distance	W_{By}
Tangential Component Gradient G_{Bx}	Peak Value	P_{GBx}
	Peak-to-Valley Value	H_{GBx}
	Peak-to-Peak Distance	W_{GBx}
Normal Component Gradient G_{By}	Peak Value	P_{GBy}
	Peak-to-Valley Value	H_{GBy}
	Peak-to-Peak Distance	W_{GBy}



(a)B_x and its characteristic parameters



(b)B_y and its characteristic parameters



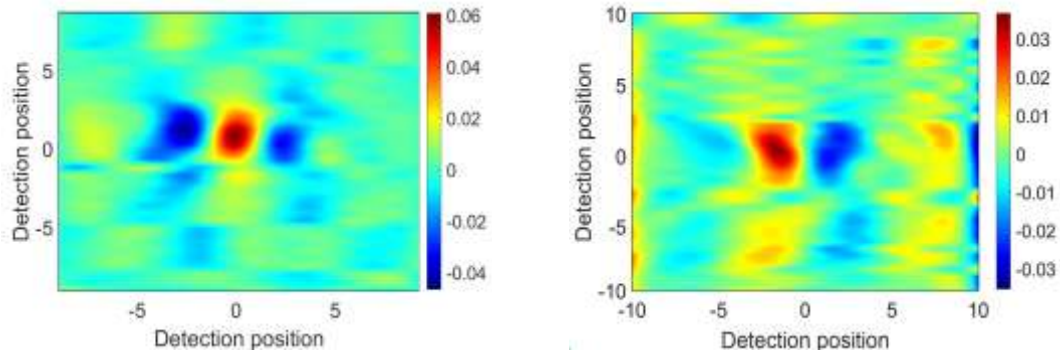
(c)G_{Bx} and its characteristic parameters (d)G_{By} and its characteristic parameters

Fig. 4. Enhanced magnetic memory signals and their characteristic parameters

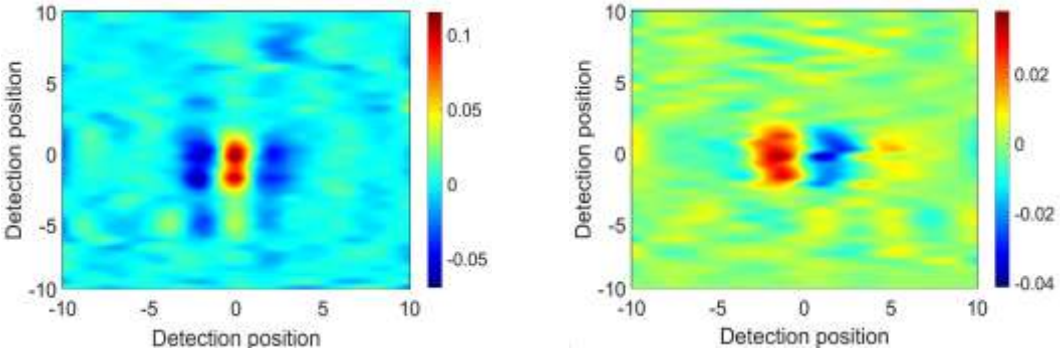
3. EFFECTS OF DEFECT PARAMETERS ON ENHANCED MAGNETIC MEMORY SIGNALS

3.1 Effects of Defect Type on Enhanced Magnetic Memory Signals

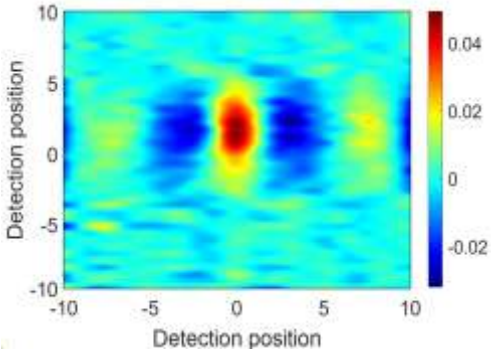
To investigate the effects of defect type on the detected signals of coiled tubing, three typical defects, namely crack, perforation, and pit defects, were considered. Comparative tests were performed on a 2 mm × 0.6 mm × 0.5 mm crack specimen, a Φ0.6 mm × 4 mm perforation specimen, and a Φ1 mm × 0.5 mm pit specimen under a stress amplitude of 1000 MPa and an excitation current of 0.5 A. Magnetic field signals were collected over a 20 mm × 20 mm region centered on the defect at a detection height of 1 mm. The tangential component B_x and normal component B_y were then fused to generate pseudocolor maps, as shown in Fig. 5.



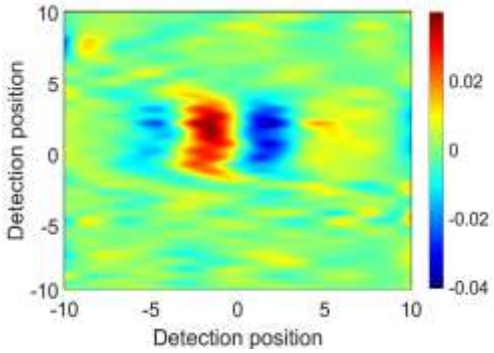
(a) Surface B_x signal of the pit defect (b) Surface B_y signal of the pit defect



(c) Surface B_x signal of the crack defect



(d) Surface B_y signal of the crack defect



(e) Surface B_x signal of the perforation defect

(f) Surface B_y signal of the perforation defect

Fig. 5. Surface magnetic field signal distributions of specimens with different defect types

The detected signals of the crack, pit, and perforation defects show similar distribution patterns. For all three defect types, the tangential component presents a positive peak at the defect center, while the normal component exhibits a typical "left peak–right valley" profile. However, clear differences are observed in the anomaly range and characteristic parameter amplitudes.

Under similar characteristic dimensions, the perforation defect produces larger characteristic parameters and the widest anomaly region compared with the pit and crack defects. This is mainly because the perforation penetrates the specimen thickness, resulting in a larger equivalent defect volume and stronger stress concentration, which further enhances the magnetic field disturbance.

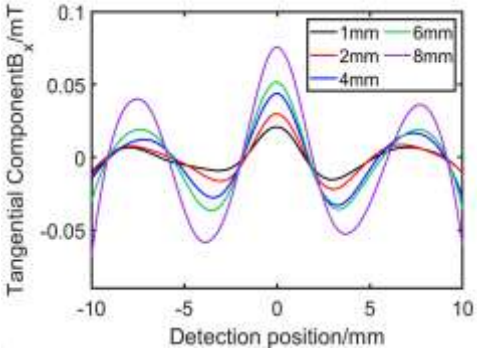
In terms of geometry, the anomaly regions of the pit and perforation defects are approximately circular, and their characteristic dimensions are closely related to the defect diameter. In contrast, the anomaly region of the crack defect extends along the crack length direction and is mainly controlled by the crack length. Therefore, defect type affects not only the signal amplitude but also the spatial distribution of the magnetic field anomaly.

3.2 Effects of Defect Size on Enhanced Magnetic Memory Signals

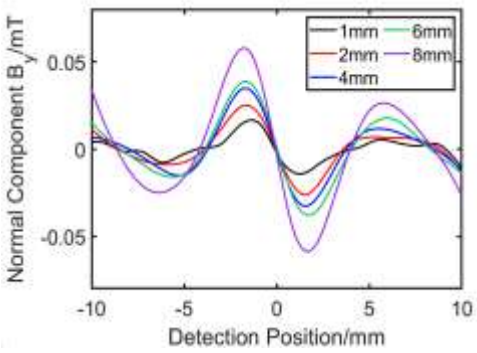
Effects of Crack Length on Enhanced Magnetic Memory Signals. Crack specimens with lengths of 1, 2, 4, 6, and 8 mm, a width of 0.6 mm, and a depth of 0.5 mm were tested to investigate the effect of crack length on the surface magnetic field distribution. The stress amplitude and excitation current were set to 1000 MPa and 0.5 A, respectively. The tangential and normal components of the detected signals were extracted along the −10 to 10 mm region at a detection height of 1 mm, and their gradients and characteristic parameters were calculated.

The processed results are shown in Fig. 6. For cracks with different lengths, the detected signals exhibit similar variation patterns near the defect. The tangential component B_x

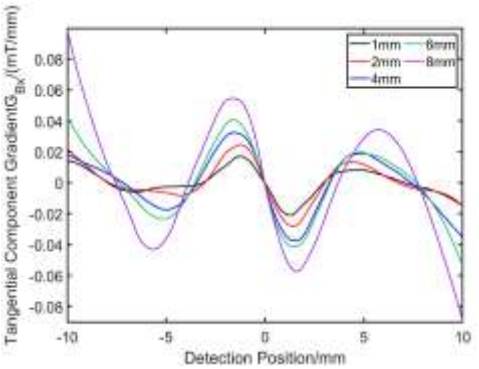
reaches a peak at the defect center, while its gradient G_{Bx} shows peak-to-valley variations on both sides of the defect and crosses zero at the defect center. The normal component B_y exhibits a peak-to-valley profile and also crosses zero at the defect center, while its gradient G_{Bx} presents a negative valley at the defect center.



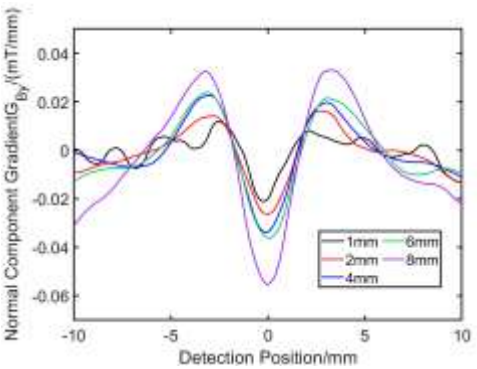
(a) Comparison of B_x under different crack lengths



(a) Comparison of B_x under different crack lengths



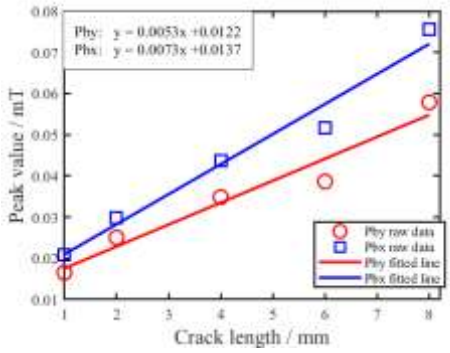
(c) Comparison of G_{Bx} under different crack lengths



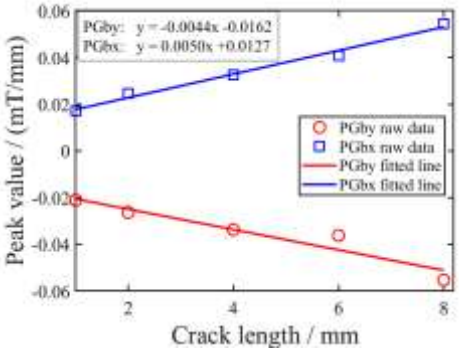
(d) Comparison of G_{By} under different crack lengths

Fig. 6. Comparison of different signal components under different crack lengths

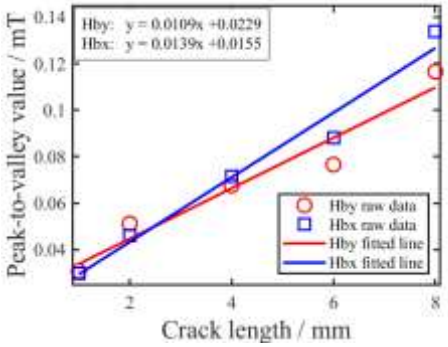
The characteristic parameters of different signal components were extracted to further analyze the effect of crack length, as shown in Fig. 7. Under the same defect width and depth, the peak value of the tangential component P_{Bx} is larger than that of the normal component P_{By}. As the crack length increases, the absolute values of the magnetic field components and their gradient characteristic parameters show an approximately linear increasing trend within the experimental range. This indicates that increasing crack length enhances the surface magnetic field anomaly of the specimen. Therefore, the tangential and normal components of the magnetic field signal can be used to characterize crack length in enhanced magnetic memory testing.



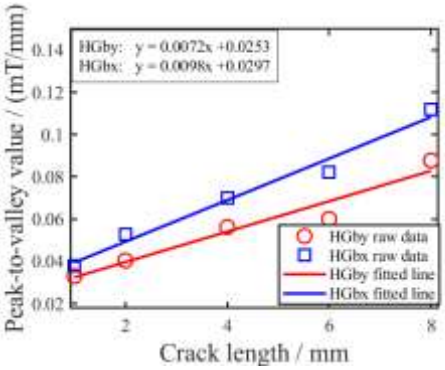
(a) Comparison of P_B under different crack lengths



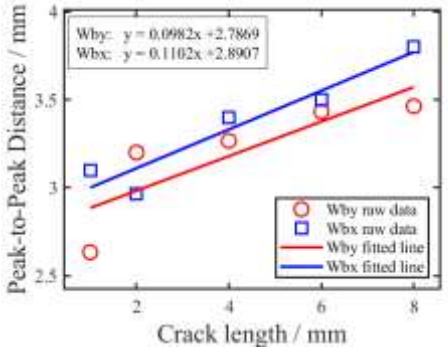
(b) Comparison of P_{GB} under different crack lengths



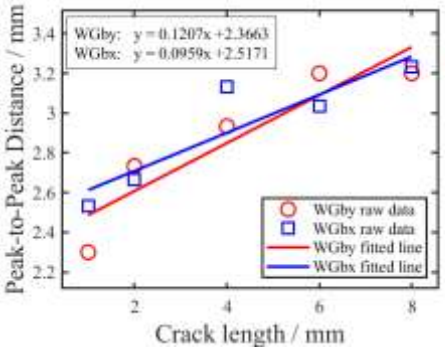
(c) Comparison of H_B under different crack lengths



(d) Comparison of H_{GB} under different crack lengths



(e) Comparison of W_B under different crack lengths



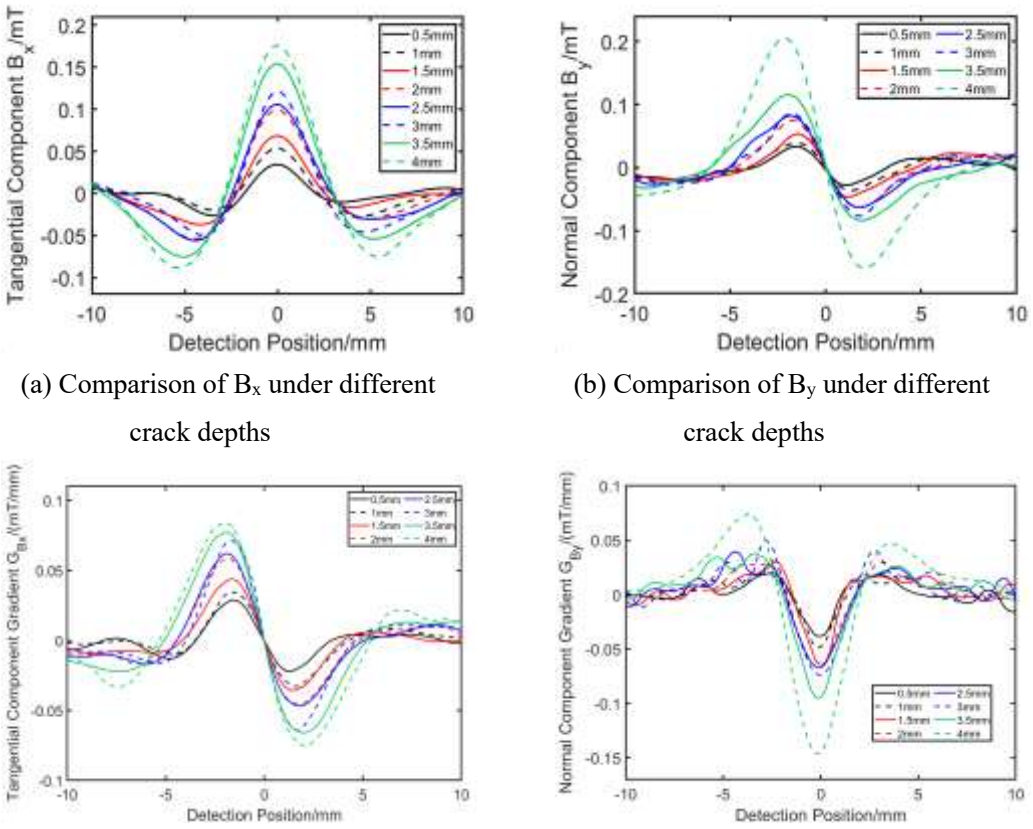
(f) Comparison of W_{GB} under different crack lengths

Fig. 7. Comparison of characteristic parameters at different crack lengths

Effects of Crack Depth on Enhanced Magnetic Memory Signals. Crack specimens with depths of 0.5, 1, 1.5, …, and 4 mm, a length of 2 mm, and a width of 0.6 mm were tested to investigate the effect of crack depth on the surface magnetic field distribution. The stress amplitude and excitation current were set to 1000 MPa and 0.5 A, respectively. The tangential and normal components of the detected signals were extracted along the −10 to 10 mm region centered on the defect at a detection height of 1 mm, and their gradients and characteristic parameters were calculated. The results are

shown in Fig. 8.

For different crack depths, the detected signals exhibit similar variation patterns near the defect. The tangential component B_X reaches a peak at the defect center, while its gradien G_{Bx} shows peak-to-valley variations on both sides of the defect and crosses zero at the defect center. The normal component B_y exhibits a peak-to-valley profile and also crosses zero at the defect center, while its gradient G_{By} presents a negative valley at the defect center.



(a) Comparison of B_x under different crack depths

(b) Comparison of B_y under different crack depths

(c) Comparison of G_{Bx} under different crack depths

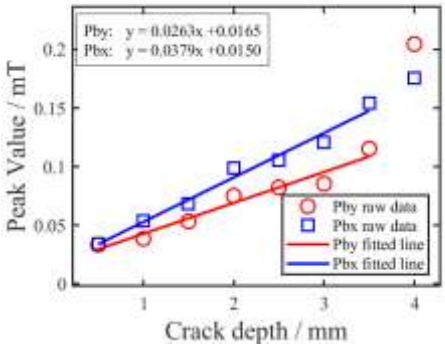
(d) Comparison of G_{By} under different crack depths

Fig. 8. Comparison of signal components at different crack depths

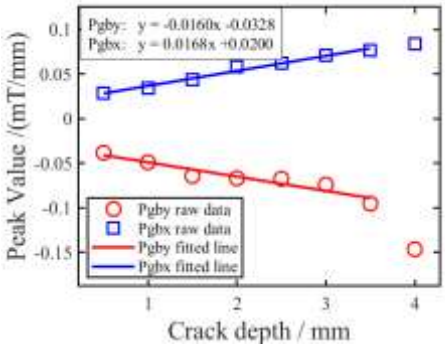
The characteristic parameters of different signal components were extracted to further analyze the effect of crack depth, as shown in Fig. 9. Within the experimental range, the absolute peak values and peak-to-valley values of the detected signals generally increase linearly with increasing crack depth. The peak-to-peak distances of different signal components also show an overall increasing trend, indicating that a greater crack depth leads to a stronger surface magnetic field response.

When the crack depth reaches 4 mm, the characteristic parameters of the normal component show an abrupt increase. This may be attributed to the crack depth approaching the specimen thickness, which significantly changes the magnetic flux path. As a result, the leakage magnetic field changes from a local disturbance state to a

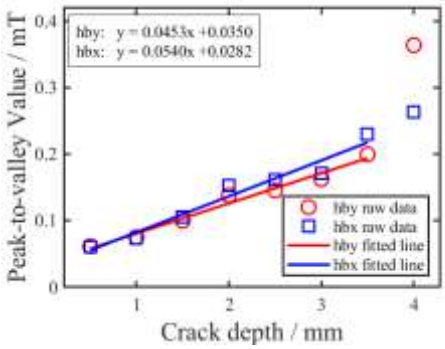
strong leakage state, leading to a sharp increase in the magnetic signal.



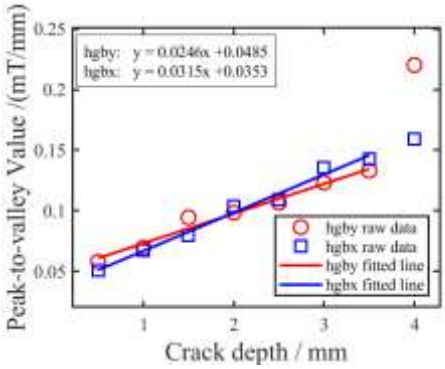
(a) Comparison of P_B under different crack depths



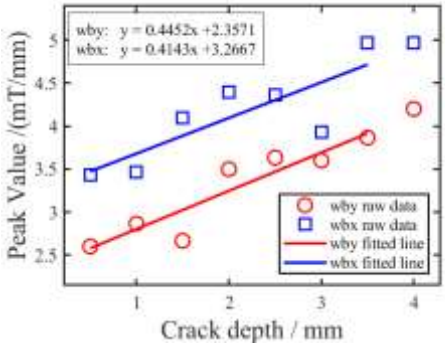
(b) Comparison of P_{GB} under different crack depths



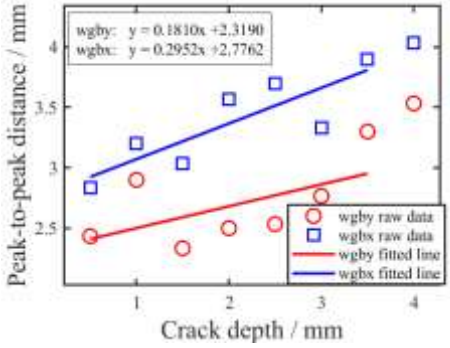
(c) Comparison of H_B under different crack depths



(d) Comparison of H_{GB} under different crack depths



(e) Comparison of W_B under different crack depths



(f) Comparison of W_{GB} under different crack depths

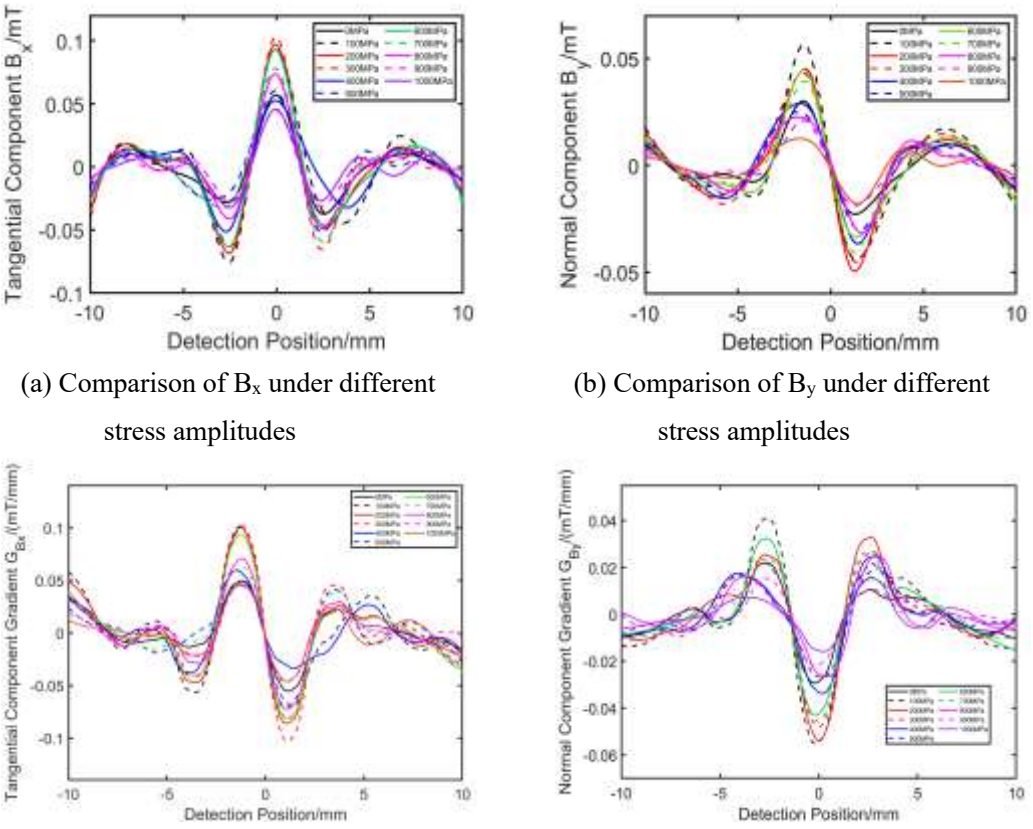
Fig. 9. Comparison of characteristic parameters at different crack depths

3.3 Effects of Loading Conditions on Enhanced Magnetic Memory Signals

Effects of Stress Amplitude on Crack Defect Detection. Stress loading tests were performed on crack specimens to investigate the variation characteristics of surface magnetic field signals under stress amplitudes ranging from 0 to 1000 MPa at an interval of 100 MPa, with an excitation current of 0.5 A. The tangential and normal

components of the magnetic field signals, as well as their gradients and characteristic parameters, were extracted from the defect-centered region at a detection height of 1 mm.

The detected signals of the crack specimen were processed, and the results are shown in Fig. 10. Under different stress amplitudes, the signals near the defect exhibit variation patterns similar to those described above.



(a) Comparison of B_x under different stress amplitudes

(b) Comparison of B_y under different stress amplitudes

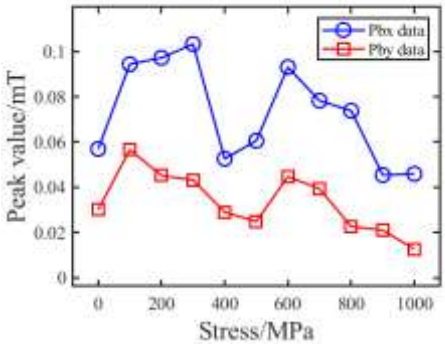
(c) Comparison of G_{Bx} under different stress amplitudes

(d) Comparison of G_{By} under different stress amplitudes

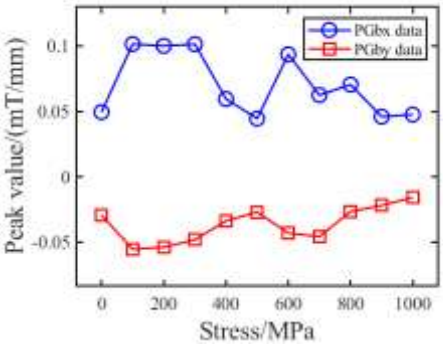
Fig. 10. Comparison of signal components under different stress amplitudes

To further analyze the effect of stress state on the surface magnetic field signals of the crack specimen, the characteristic parameters of the tangential and normal components were extracted under different stress amplitudes, as shown in Fig. 11. Although the characteristic parameters show local fluctuations, they exhibit a generally consistent staged evolution behavior. In the 0–200 MPa stage, the parameters increase rapidly, with H_{Bx}, P_{Bx}, and P_{GBx} increasing by 94.8%, 81.4%, and 102.2%, respectively. In the 200–500 MPa stage, the parameters decrease overall, which may be related to the enhanced pinning of magnetic domain walls. In the 500–800 MPa stage, the parameters increase again and reach peak values near 800 MPa, indicating that the local stress concentration at the crack tip and magnetic domain rearrangement become most pronounced during the elastic–plastic transition of CT130. In the 800–1000 MPa stage,

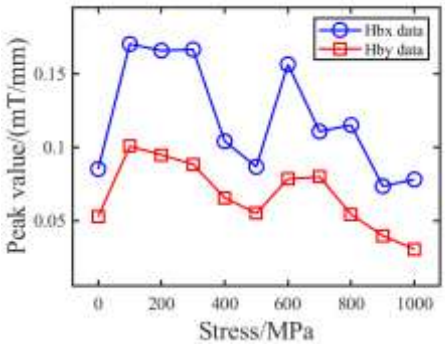
the parameters decrease again, suggesting that dislocation multiplication and microplastic deformation gradually dominate the magnetic response.



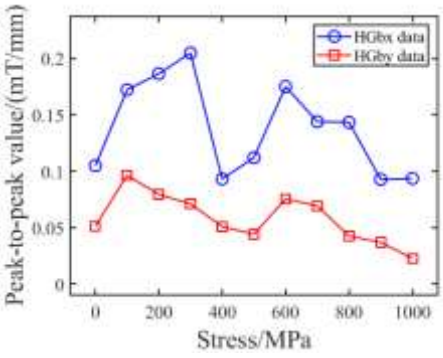
(a) Comparison of P_x under different stress amplitudes



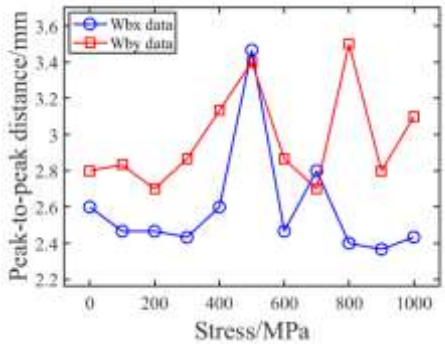
(b) Comparison of P_{GB} under different stress amplitudes



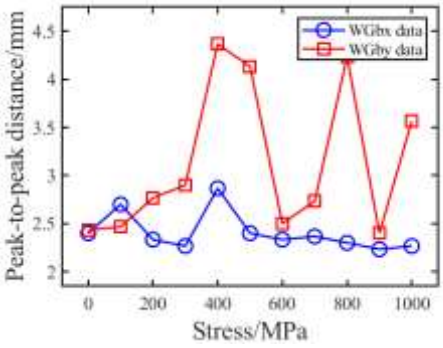
(c) Comparison of H_B under different stress amplitudes



(d) Comparison of H_{GB} under different stress amplitudes



(e) Comparison of W_B under different stress amplitudes

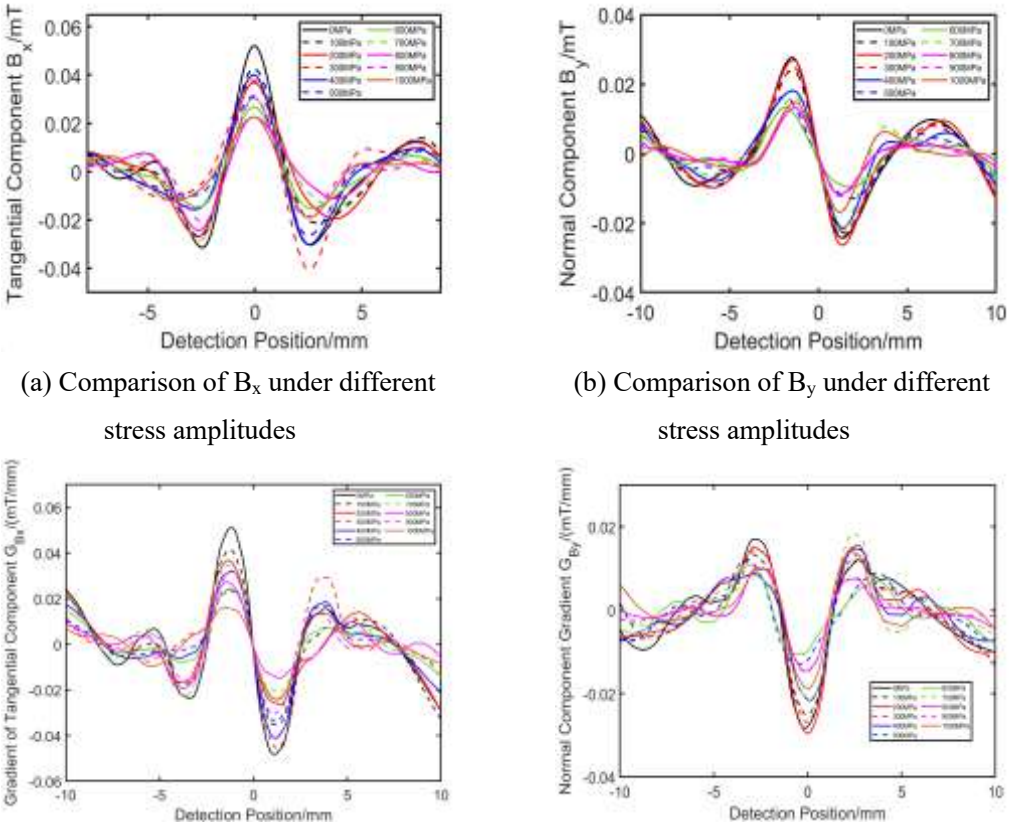


(f) Comparison of W_{GB} under different stress amplitudes

Fig. 11. Comparison of characteristic parameters under different stress amplitudes

Effects of Stress Amplitude on Pit Defect Detection. Similar stress loading tests were conducted on pit specimens under the same experimental conditions. The detected signals of the pit specimen were processed, and the results are shown in Fig. 12. Under different stress amplitudes, the signals near the defect exhibit variation patterns

generally consistent with those described above.



(a) Comparison of B_x under different stress amplitudes

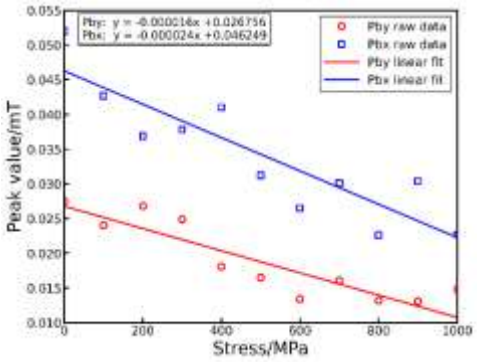
(b) Comparison of B_y under different stress amplitudes

(c) Comparison of G_{Bx} under different stress amplitudes

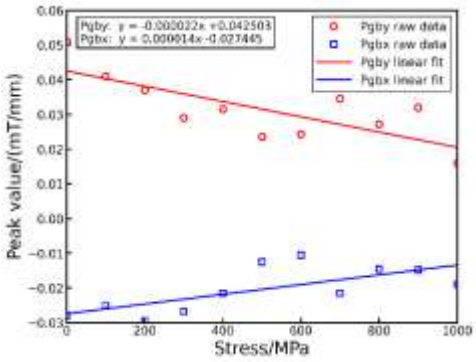
(d) Comparison of G_{By} under different stress amplitudes

Fig. 12. Comparison of signal components under different stress amplitudes

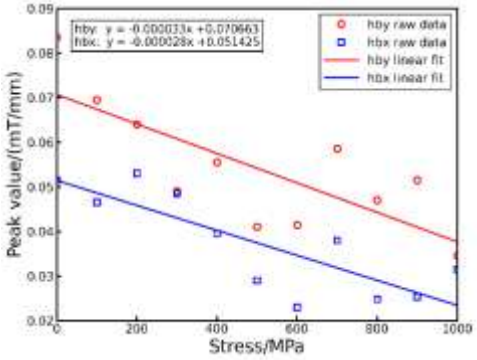
To further analyze the effect of stress state on the surface magnetic field signals of the pit specimen, the characteristic parameters of the tangential and normal components were extracted under different stress amplitudes, as shown in Fig. 13. Under the same testing condition, the peak value of the tangential component P_{Bx} is larger than that of the normal component P_{By}, and the peak value of the tangential component gradient P_{GBx} is also larger than the absolute value of the normal component gradient P_{GBy}. With increasing load, the peak values P_B, peak-to-valley values H_B, gradient peak values P_{GB}, and gradient peak-to-valley values H_{GB} generally show a linear decreasing trend. In contrast, the peak-to-peak distances W_B and W_{GB} do not exhibit a clear variation trend with increasing load.



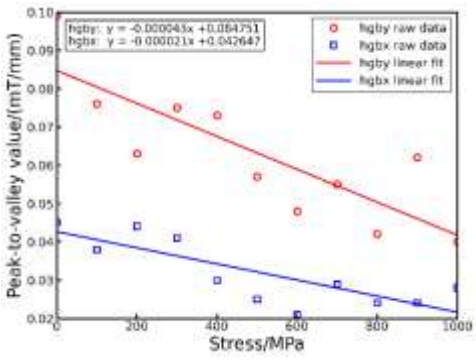
(a) Comparison of P_B under different stress amplitudes



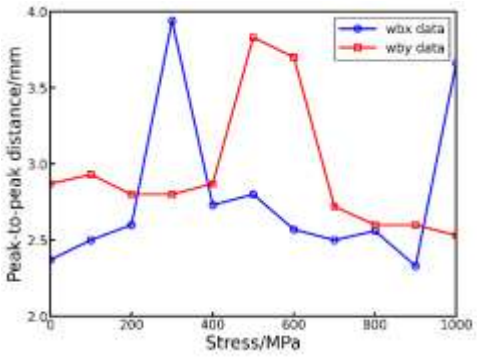
(b) Comparison of P_{GB} under different stress amplitudes



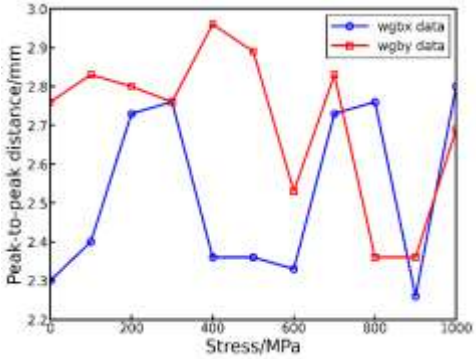
(c) Comparison of H_B under different stress amplitudes



(d) Comparison of H_{GB} under different stress amplitudes



(e) Comparison of W_B under different stress amplitudes

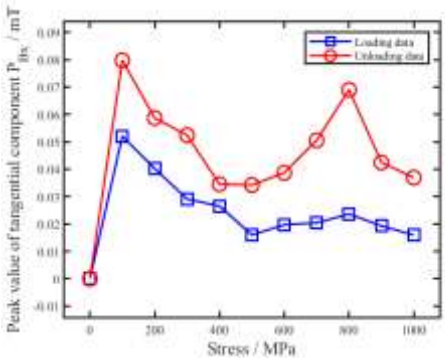


(f) Comparison of W_{GB} under different stress amplitudes

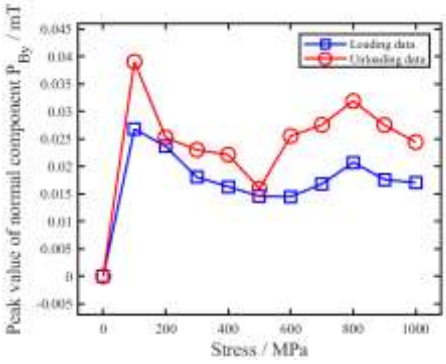
Fig. 13. Comparison of characteristic parameters under different stress amplitudes

Effects of Loading–Unloading Conditions on Enhanced Magnetic Memory Signals. To simulate repeated loading–unloading conditions during coiled tubing service, tensile loading–unloading tests were conducted on specimens with a defect size of Φ0.6 × 4 mm. To analyze the effect of loading condition on the detected signals, the peak and peak-to-valley characteristic parameters of the tangential and normal components near the defect were extracted and compared under different stress states. The results are

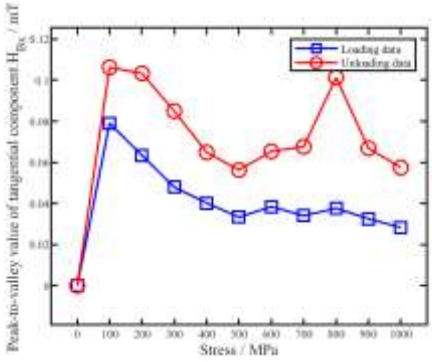
shown in Fig. 14.



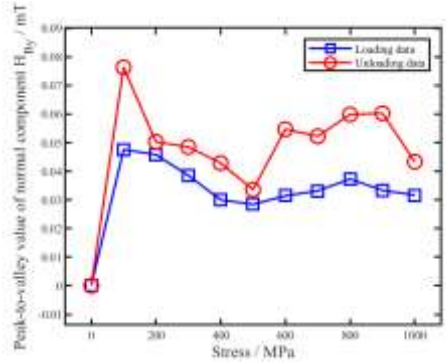
(a) Comparison of P_{Bx} under loading and unloading conditions



(b) Comparison of P_{By} under loading and unloading conditions



(c) Comparison of H_{Bx} under loading and unloading conditions



(d) Comparison of H_{By} under loading and unloading conditions

Fig. 14. Comparison of signal components under loading and unloading conditions

Under both online loading and unloading conditions, the magnetic field characteristic parameters exhibit similar staged evolution behavior: a rapid increase at low stress levels, a gradual decrease at medium stress levels, followed by a secondary increase and subsequent decrease at high stress levels. Compared with the online loading condition, the unloading condition generally produces higher characteristic parameter values. Specifically, at around 100 MPa, H_{Bx} and P_{Bx} under unloading conditions are 34.3% and 53.0% higher than those under loading conditions, respectively, indicating that residual magnetization remains in the material after unloading. With increasing stress, local peaks appear near 800 MPa under both loading and unloading conditions. This stress level corresponds to the elastic–plastic transition stage of CT130, suggesting that enhanced magnetic memory signals are sensitive to internal stress states and damage evolution in the material.

4 CONCLUSIONS

Based on the established online enhanced magnetic memory testing system, the effects of defect parameters and loading conditions on the detected signals of coiled tubing were investigated. The main conclusions are as follows:

(1) As the crack length and depth increase, the magnetic field characteristic parameters show an approximately linear increasing trend, with the R^2 values of all fitting models higher than 0.9. When the crack length increases from 1 mm to 8 mm, P_{Bx} and P_{By} increase by 263.7% and 161.9%, respectively. When the crack depth increases from 0.5 mm to 4 mm, P_{Bx} and P_{By} increase by 494.9% and 233.6%, respectively. The fitting slope corresponding to crack depth is larger than that corresponding to crack length, indicating that crack depth has a more significant effect on local magnetic field anomalies.

(2) Different defect types all produce obvious magnetic field anomalies near the defect region, but they do not change the overall distribution pattern of the magnetic field signal. As the defect volume increases, the magnetic anomaly region expands. Among the extracted parameters, peak-value and gradient-related parameters are more sensitive to defect size variation.

(3) Under online loading and unloading conditions, the magnetic field characteristic parameters exhibit similar staged evolution behavior. However, the parameter values under unloading conditions are generally higher than those under loading conditions. At 100 MPa, P_{Bx} under unloading conditions is 53.0% higher than that under loading conditions, indicating that obvious residual magnetization remains in the material after unloading. This suggests that enhanced magnetic memory signals have a strong historical memory effect.

(4) With increasing stress amplitude, the magnetic field characteristic parameters exhibit clear staged evolution behavior. They increase rapidly in the 0–200 MPa stage, decrease gradually in the 200–500 MPa stage, increase again in the 500–1000 MPa stage, and reach a local peak near 800 MPa before decreasing again. This stress range corresponds to the elastic–plastic transition stage of CT130, suggesting that local stress concentration at the crack tip, magnetic domain rearrangement, and microplastic deformation have important effects on the magnetic response. Overall, enhanced magnetic memory signals can sensitively reflect the internal stress state and local damage evolution of defective coiled tubing.

ACKNOWLEDGMENTS

We would like to thank the laboratory staff for their assistance in the experimental testing and data acquisition.

AUTHOR CONTRIBUTIONS

T.H. conceived the study, conducted the experiments, analyzed the data, and drafted the manuscript. Y.L. contributed to the experimental design, data interpretation, and manuscript revision. Z.L. prepared the figures and assisted with data analysis and visualization. W.J. participated in data collection, validation, and experimental testing. A.M. assisted with specimen preparation and experimental investigation. X.L. supervised the project, provided technical guidance, and revised the manuscript. All authors reviewed and approved the final manuscript.

DATA AVAILABILITY

The datasets generated and/or analyzed during the current study are available from the corresponding author on reasonable request.

FUNDING

This study was supported by National Natural Science Foundation of China Youth Fund under Grant 52404004，Sichuan Science and Technology Program 2024ZYD0142，2024YFNH0022.

CONFLICT OF INTEREST

The authors declare that they have no conflicts of interest.

REFERENCES

[1] Li X.Q., Fan J.C., Zhao K.P., et al. Experimental study on fatigue damage of coiled tubing based on metal magnetic memory testing. Journal of Safety Science and Technology, 2013, 9(6): 54–57. (in Chinese)

[2] Duan Z.X., Ren S.K., Xi X.W., et al. Magnetizing reversal characteristic of 40Cr steel during stress-magnetizing process. Journal of Iron and Steel Research, 2016, 28(1): 77–80. (in Chinese)

[3] Liu Z.F., Fei Z.Y., Huang H.H., et al. Study on Strengthening Mechanism of Excitation Magnetic Field to Stress-magnetization Coupling Effects. China Mechanical Engineering, 2018, 29(9): 1108–1114. (in Chinese)

[4] Fu M.L., Bao S., Bai S.Z., et al. Influence of tensile stress on magnetic memory signal in Q345 steel with different thicknesses. Journal of Harbin Institute of Technology, 2017, 49(6): 178–182. (in Chinese)

[5] Ren S.K., Huang Y., Xi X.W., et al. Magnetizing Reversal Effect under Torsion Action of Q235 Steel. Nondestructive Testing, 2016, 38(11): 30–33. (in Chinese)

[6] Ni J.L., Fan J.C., Hu Z.B., et al. Quantitative Study on Magnetic Memory Detection Signal for Coiled Tubing Damage. China Petroleum Machinery, 2017, 45(12): 88–91. https://doi.org/10.16082/j.cnki.issn.1001-4578.2017.12.018. (in Chinese)

[7] Jia D., Sun L., Chen Y.M., et al. The metal magnetic memory effect of X80 pipeline steel under tension load. China Measurement & Test, 2017, 43(1): 17–22. (in Chinese)

[8] Bai Y., Xu F., Qiao A.T. Relationship Between Residual Plastic Deformation and Metal Magnetic Memory Signals of Specimens. Journal of Materials Engineering, 2013, (8): 42–49. (in Chinese)

[9] Leng J.C., Xu M.Q., Li J.W., et al. Relationship between magnetic memory signal and stress. Journal of Harbin Institute of Technology, 2010, 42(2): 232–235. (in Chinese)

[10] Xu K.S., Qiu X.Q., Jiang H., et al. Influence of hole diameter and stress concentration on metal magnetic memory signal. Journal of Magnetic Materials and Devices, 2016, 47(1): 49–53. (in Chinese)

[11] Xu K.S., Qiu X.Q., Liu J.T., et al. Effect of heat treatment and stress concentration on magnetic memory signal in Q345R steel. Transactions of Materials and Heat Treatment, 2016, 37(5): 210–215. https://doi.org/10.13289/j.issn.1009-6264.2016.05.037. (in Chinese)

[12] Li H.B., Ren N., Xian L.Y., et al. Performance and Field Application of Domestic CT130 Coiled Tubing. Welded Pipe and Tube, 2020, 43(10): 23–28. (in Chinese)

[13] Hamad R.K., Rashid T.A. GOOSE algorithm: a powerful optimization tool for real-world engineering challenges and beyond. Evolving Systems, 2024, 15: 1249–1274.